

# An Eddy Current Probe for the Detection of Subsuperficial Defects of Any Orientation

Federico Carere<sup>1</sup>, Member, IEEE, Alessandro Sardellitti<sup>2</sup>, Member, IEEE, Andrea Bernieri<sup>3</sup>, Member, IEEE, Luigi Ferrigno<sup>4</sup>, Senior Member, IEEE, Silvia Sangiovanni<sup>5</sup>, and Marco Laracca<sup>6</sup>, Member, IEEE

**Abstract**—The article introduces a novel four-coil probe designed for eddy current (EC) nondestructive testing (NDT) on conductive materials. The key innovation lies in its capability to identify small surface and subsurface cracks regardless of their orientation. This is achieved through a suitable probe developed using two pairs of exciting coils that allow to generate two orthogonal magnetic fields. Using two excitation currents with an amplitude modulation approach, a rotation of the ECs induced in the conductive sample is obtained. This novel approach ensures the effective detection of deep and arbitrarily oriented cracks. Both numerical tests and experimental evaluations were employed to assess the performance of the proposed probe. The probe's effectiveness was particularly observed in detecting a buried crack measuring 5 mm in length, 1 mm in height, and 0.1 mm in thickness at depths up to 3 mm in an aluminum plate. The results demonstrated the robustness of the probe's detection capability, affirming its potential as a reliable tool for NDT in industrial applications.

**Index Terms**—Any orientation defects, buried cracks, defect characterization, defect detection, eddy current testing (ECT), finite element method, rotating eddy current (REC), rotating magnetic field.

## I. INTRODUCTION

THE eddy current testing (ECT) is a method in the field of nondestructive testing (NDT) based on the principle of Faraday's electromagnetic induction. In recent years, this method has attracted considerable interest in many areas. The ECT methods are adopted for structural inspections, as in the case of turbine blades in the aerospace sector [1], [2], [3], tubes' inspection [4], [5], [6], [7], thickness measurement of laminates or coatings [8], [9], [10], identification of corrosion damages [11], verification of materials treatment techniques, and bolt hole inspections. The relevant interest in ECT techniques for the analysis of the structural degradation status is

Manuscript received 8 January 2024; revised 12 April 2024; accepted 17 April 2024. Date of publication 30 April 2024; date of current version 9 May 2024. This work was supported by the Project "Sensors and Measurements Methods for aware BATteries MAnagement in uninterruptible safety-critical and mission-critical applications – BATMAN" CUP H53D23000600006 funded by EU in NextGenerationEU Plan through the Italian "Bando Prin 2022 - D.D. 104 del 02-02-2022" by MUR. The Associate Editor coordinating the review process was Dr. Chao Tan. (Corresponding author: Alessandro Sardellitti.)

Federico Carere, Silvia Sangiovanni, and Marco Laracca are with the Department of Astronautics, Electrical and Energy Engineering, Sapienza University of Rome, 00184 Rome, Italy (e-mail: federico.carere@uniroma1.it; silvia.sangiovanni@uniroma1.it; marco.laracca@uniroma1.it).

Alessandro Sardellitti, Andrea Bernieri, and Luigi Ferrigno are with the Department of Electrical and Information Engineering, University of Cassino and Southern Lazio, 03043 Cassino, Italy (e-mail: alessandro.sardellitti@unicas.it; bernieri@unicas.it; ferrigno@unicas.it).

Digital Object Identifier 10.1109/TIM.2024.3395324

due to the noncontact, low measurement time, and high defect detection sensitivity.

In general, ECT methods are able to detect a defect in a conductive material by exploiting the reaction magnetic field generated by the eddy currents (ECs), in the presence of changes in the material conductivity due to the defect. One or more coils, located over the material at a suitable distance named "lift-off" [12], supplied by suitable excitation currents (sinusoidal, multifrequency [13], [14], or pulsed signals [15], [16], [17] are typically used) allow the generation of a primary magnetic field. ECs are then induced in the conductive material under test generating a secondary magnetic field. The total magnetic field, consisting of the superposition of the primary and secondary magnetic fields, is usually measured by means of receiving coils or magnetic sensors, such as superconducting quantum interference devices (SQUIDS), Hall-effect sensors, and magnetoresistive sensors, such as giant magnetoresistance (GMR) and tunnel magnetoresistance (TMR). The last ones have been adopted in many research activities in the last years due to their small size, high-frequency operation, and good sensitivity [18], [19]. This article is focused on a particular class of defects, named cracks, characterized by the presence of one dimension that can be considered negligible with respect to the others. One of the major open issues in crack detection is related to its orientation with respect to the EC path direction. Unfavorable orientations give rise to a reduction in the detection sensitivity that affects the ECT performance, especially in the presence of small and buried cracks [20], [21], [22], [23], [24], [25], [26], [27], [28], [29], [30], [31], [32], [33].

In fact, the best detection capability of an ECT probe is, in general, reached when the EC path and the main dimension of the defect are orthogonal (thanks to a larger variation of the ECs due to the defect presence), whereas, moving away from this condition, the performance reduces reaching the minimum when the orientation of the defect and the EC path are parallel. The simplest solution to address this problem is to repeat the test by spatially rotating the probe 90°. However, this method is time-consuming and does not result in the best detection sensitivity.

This problem was investigated by the scientific community. Some researchers proposed the EC array as a promising solution due to the possibility of reducing the inspection time and exploiting suitable multifrequency analysis. At the same time, this solution requires complex equipment and a longer setup time [20], [21]. In [23] and [24], magnetic field imaging techniques are adopted with magnetoresistive sensor array to

achieve high resolution. In [23], a right-angle isosceles triangle excitation coil is realized to detect arbitrarily oriented defects. In [24], ECT is realized by means of an array of 64 TMR sensors with a three-phase excitation system, which requires a size of about  $98 \times 33$  mm. The authors demonstrated that the novel probe is able to detect in an aluminum sample a superficial defect with a length of 1 mm, a width of 0.2 mm, and a height of 1 mm.

Another solution to make the probes more sensitive to arbitrarily oriented defects is the so-called rotating EC (REC) methodology [26], [27], [28], [29], [30], [31], [32]. The traditional REC methodology is based on two orthogonal coils supplied by sinusoidal currents with the same amplitude and a  $90^\circ$  phase shift. In this way, during one excitation signal period, the ECs perform a complete  $360^\circ$  spatial rotation, thus ensuring the possibility of orthogonal interaction between the defect and the ECs.

In [26], the impact of defect orientation is addressed by improving the traditional REC method. The proposed probe is based on two orthogonal arranged rectangular coils, as excitation coils, and another pair as pick-up coils. The authors implement an oscillatory method that induces a complete variation of the ECs' orientation and amplitude during one period of the excitation currents, reaching good detecting performances also in the case of ferromagnetic samples.

Other studies apply the REC technique for the detection of complex cracks characterized by different shapes; for example, Ge et al. [27], [28] investigate the EC image method that represents the defect as current dipoles [29] to improve the signal to noise ratio (SNR) of defect images obtained with an REC technique. In [30], a novel differential ECT probe is proposed, in which the EC rotation is realized by means of four-square driver coils. The benefits of this probe are linked to the detection performance on complex surfaces, like the case of rail treads, in which the lift-off variation is a relevant issue. Nonetheless, the authors state that the SNR should be improved, and the detection capability of the probe decreases with the decrease in the angle between the defect and the EC path. In [31], the REC technique is applied by means of two pairs of focusing subprobes placed orthogonally to each other. The main target of this study is related to analyzing the impact of the tilt angle of the two subprobes in obtaining a concentration of the magnetic field in the defect zone. This focusing effect is able to increase the SNR values in the defects' detection.

The literature review related to the REC techniques highlighted that in most of the studies, these are applied in the case of superficial defects. In [32], an REC technique is applied to the case of a small and subsuperficial crack in an aluminum multilayer structure. Nonetheless, in the article, the authors state that the SNR values are not sufficient to obtain clear maps for this defect.

The aim of this article is to face the problem of the detection sensitivity of subsurface defects of any orientation. The authors started from their previous studies [18], [33] in which they proposed a double coil ECT probe, demonstrating its effectiveness in detecting small and subsuperficial defects. After a preliminary study in a simulation environment [34],

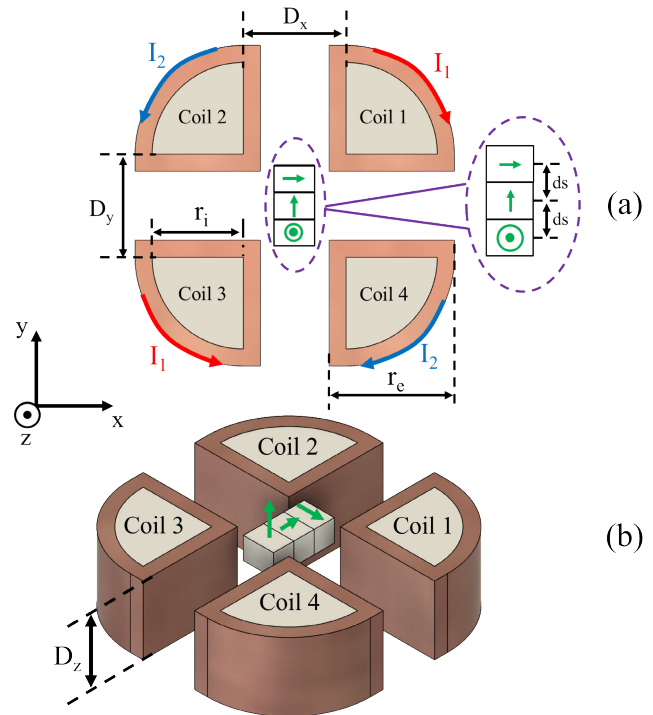


Fig. 1. Representation of the proposed EC probe and ECs rotation. (a) 2-D representation. (b) 3-D representation.

in this article, the authors designed a novel four quadrant (4Q) ECT probe to extend the subsuperficial detection capability of the previous double coil probe regardless of the defect orientation exploiting the REC technique.

The article is organized as follows. Section II illustrates the novel probe realization; Section III shows the considered test bed and experimental/numerical setup. Section IV reports numerical and experimental results. Finally, Section V summarizes the conclusions and future development.

## II. PROPOSED PROBE

As described above, the design of the novel 4Q ECT probe started from the suitability, in detecting buried cracks, of the double coil probe proposed by Betta [18] and Bernieri et al. [33]. As depicted in Fig. 1, the new probe shares the same excitation strategy, but it uses four quarter circle-shape excitation coils in order to realize the ECs rotation.

The internal dimension ( $r_i$ ) of the four coils was fixed as 8 mm, while the external dimension ( $r_e$ ) was fixed as 11 mm. The interdistances  $D_x$  and  $D_y$  along  $x$ - and  $y$ -axes, respectively, were fixed as 15 mm, while the height of the coils is equal to 10 mm ( $D_z$ ). The number of turns is equal to 150 for each coil. The optimal solution in terms of sensor technologies was identified in the TMR sensors (Multidimension Technology TMR2905 [19]) for their suitable sensitivity in low magnetic field conditions ( $50 \sim 60$  mV/V/G), small sizes ( $3 \times 3 \times 0.75$  mm), and their good metrological performance already shown in ECT methods (see [18]). The small size of the TMR2905 allowed the location of the three magnetic field sensitivity points at a distance  $ds$  equal to 3 mm (see Fig. 1).

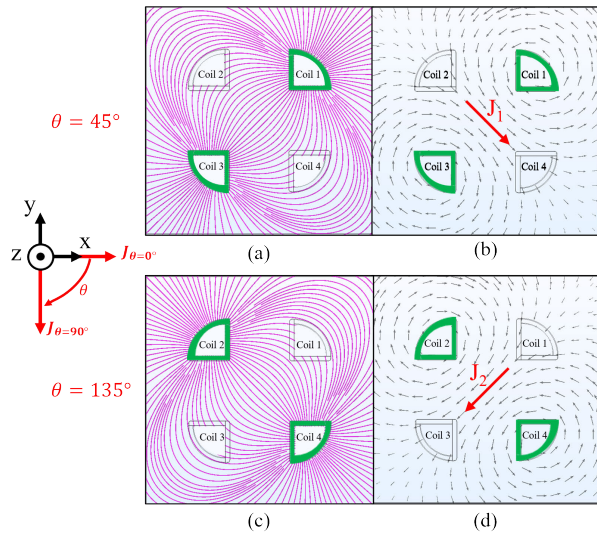


Fig. 2. Graphical representation of the magnetic flux lines (left) and of the ECs path (right) calculated in COMSOL environment for orientation angles  $\theta$  of the ECs equal to (a) and (b)  $45^\circ$  and (c) and (d)  $135^\circ$ .

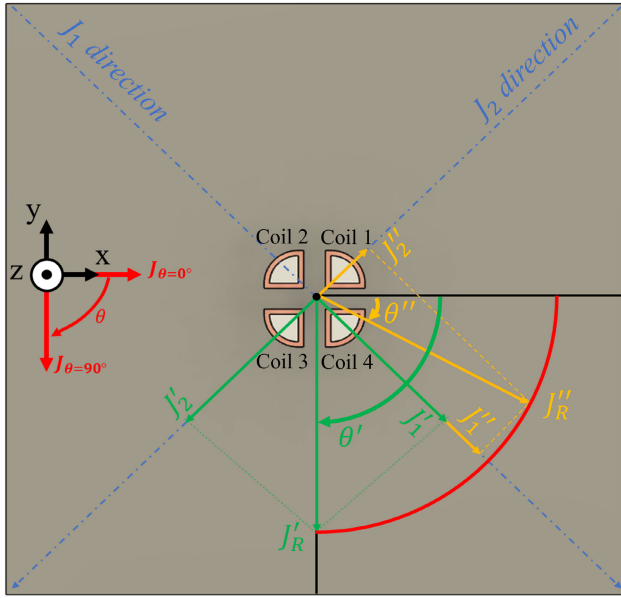


Fig. 3. Graphical representation of the adopted REC technique  $\theta' = 90^\circ$  and  $\theta'' = 30^\circ$  cases.

The coils 1 and 3 are supplied by the same current amplitude  $I_1$  circulating in opposite directions. The excitation of coils 1 and 3 generates a time-variable magnetic field characterized by the flux lines shown in Fig. 2(a). It induces EC in the specimen under test, following the path represented in Fig. 2(b). In this condition, the ECs' path ( $J_1$ ) has a main orientation  $\theta$  of  $45^\circ$  (according to the reference system in Fig. 2) in the area of the specimen positioned under the center point of the four coils.

The same excitation strategy is adopted for coils 2 and 4. They are supplied by the current  $I_2$ , which is characterized by the same amplitude of  $I_1$  and circulates in opposite directions with respect to coils 1 and 3. As a consequence, the time-variable magnetic field, characterized by the flux lines

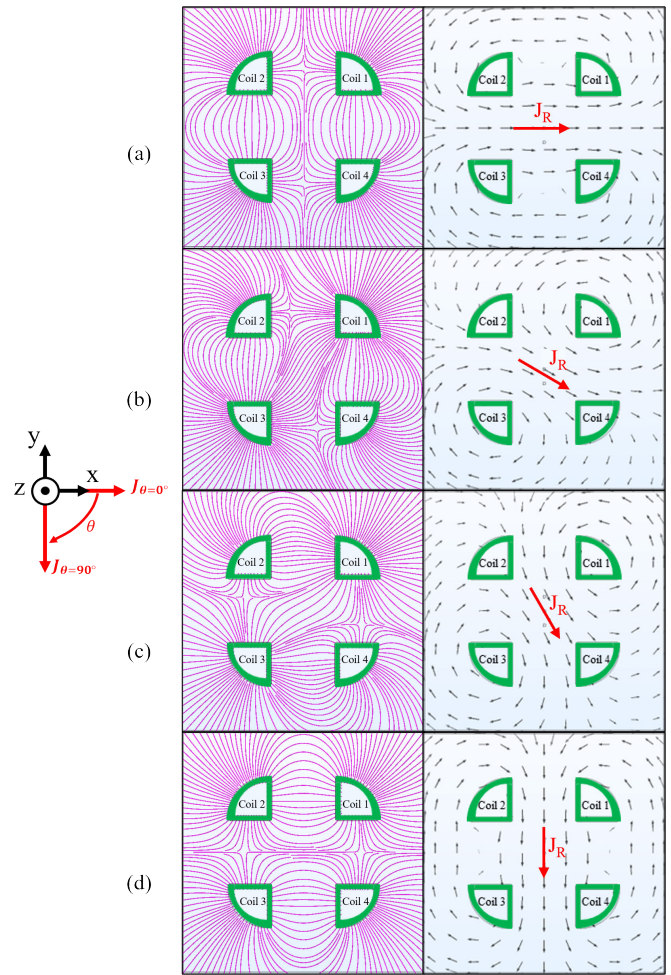


Fig. 4. Graphical representation of the magnetic flux lines (left) and of the ECs path (right) calculated in COMSOL environment for different values of  $\theta$  (a)  $0^\circ$ , (b)  $30^\circ$ , (c)  $60^\circ$ , and (d)  $90^\circ$ .

shown in Fig. 2(c), is generated. In this condition, the induced EC path is shown in Fig. 2(d) and has a main orientation  $\theta$  of  $135^\circ$  ( $J_2$ ) in the area of the specimen positioned under the center point of the four coils. Since the two pairs of coils 1-3 and 2-4 are symmetrically developed and share the same geometrical and constructive characteristics, the ECs paths  $J_1$  and  $J_2$  are orthogonal to each other. If the two pairs of coils are supplied simultaneously, the resultant EC path  $J_R$  is the superposition of  $J_1$  and  $J_2$ . Since the EC magnitudes ( $J_1$  and  $J_2$ ) are proportional to the magnitude of the excitation currents ( $I_1$  and  $I_2$ ), it is possible to rotate  $J_R$  by adjusting the amplitude of  $I_1$  and  $I_2$  according to (1) and (2). Fig. 3 shows a representation of the  $J_R$  rotation considering two examples for the choices that can be made on  $J_1$  and  $J_2$

$$I_1 = I_b \cdot \cos(45^\circ - \theta) \tag{1}$$

$$I_2 = I_b \cdot \sin(45^\circ - \theta). \tag{2}$$

In (1) and (2),  $I_b$  is named the base current, whereas  $\theta$  is the angle representative of the orientation of  $J_R$ . Applying the trigonometric addition and subtraction formulas to (1) and (2) and neglecting the multiplication constant  $\sqrt{2}/2$  (that affects both equations), the relationships between the excitation currents  $I_1$  and  $I_2$  and the rotation angles  $\theta$  of the ECs can be

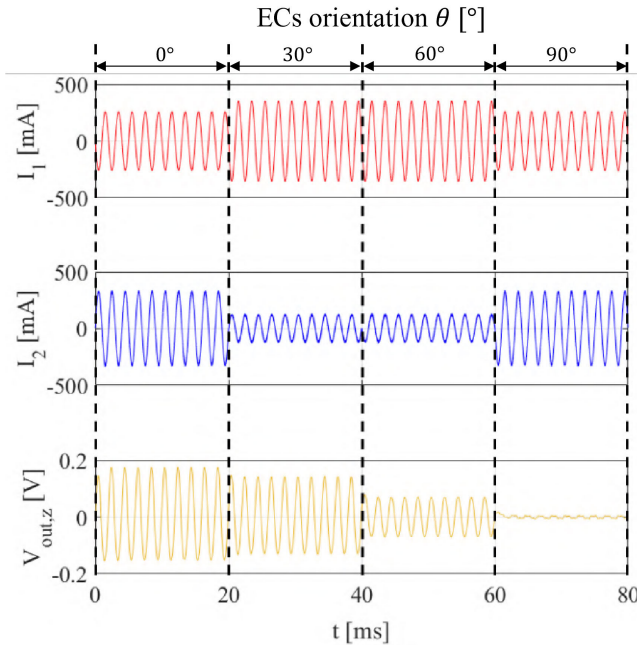


Fig. 5. Example of the excitation signal's waveform ( $I_1$  and  $I_2$ ) and the corresponding output voltage of the TMR sensitive to the  $z$ -component ( $V_{\text{out},z}$ ) of the magnetic field in the case of EC's orientation  $\theta$  of  $0^\circ$ ,  $30^\circ$ ,  $60^\circ$ , and  $90^\circ$ .

written as follows:

$$I_1 = I_b \cdot [\cos(\theta) + \sin(\theta)] \quad (3)$$

$$I_2 = I_b \cdot [-\cos(\theta) + \sin(\theta)]. \quad (4)$$

In Fig. 4, some examples of both the magnetic flux and the EC lines (calculated in COMSOL environment) supplied simultaneously by the two pairs of coils are shown. Different  $J_R$  orientations have been considered applying (3) and (4). It is possible to highlight that, depending on the values of  $\theta$ , the magnetic field fluxes generated by the coils create different tubes of flux. As an example, in the case of  $\theta$  equal to  $0^\circ$ , coils 1-4 and coils 2-3 are involved by the same magnetic tube of flux [see Fig. 4(a)]; in the case of  $\theta$  equal to  $90^\circ$ , the magnetic tube of flux involves coils 1-2 and coils 3-4 [see Fig. 4(d)].

The ECs induced in the specimen under test generate a secondary magnetic field. The total magnetic field, composed of the primary magnetic field (generated by the excitation coils) and the secondary magnetic field, is sensed by TMR sensors that provide an output voltage amplitude proportional to the amplitude of the magnetic field. Fig. 5 shows an example of the waveform of the excitation currents ( $I_1$  and  $I_2$ ) and the output voltage of the TMR sensor detecting the  $z$ -component ( $V_{\text{out},z}$ ) of the magnetic field in the case of positioning the probe over a specimen area far from the crack. Under these conditions, the sensed values of the magnetic field represent the reference values to be used to evaluate the magnetic field variations due to the defect presence.

In this example, the excitation currents  $I_1$  and  $I_2$  are varied four times in order to obtain the EC's orientation  $\theta$ , respectively, at  $0^\circ$ ,  $30^\circ$ ,  $60^\circ$ , and  $90^\circ$ . In the case where the sensitivity point of the magnetic field sensor relative to the  $z$ -component of the magnetic field is in the center of the four coils, and considering the ideal conditions under which the

symmetry of the probe is ensured, the reference value on the  $z$ -axis should not be influenced by the orientation of the ECs since it is realized in the  $x$ - $y$  spatial plane. The amplitude variations of the TMR output signal, as shown in Fig. 5, related to the ECs' orientation are due to 3 mm of asymmetry in the position of the  $z$ -axis sensitivity point.

It is important to remark that applying the proposed amplitude modulation [see (3) and (4)], it is possible to change the orientation of the resultant component  $J_R$ , holding its amplitude unchanged. This is a meaningful aspect since in this way the tests are made at all the ECs' orientation angles with the same EC amplitude, granting the same detection capability.

In the other REC techniques, the EC rotation is linked to the time evolution of the excitation currents in one period. In contrast, the proposed approach allows us to fix the orientation angle with respect to the time evolution of the excitation currents, executing a discrete rotation of  $J_R$ . This feature is characterized by a drawback related to the discretization of the EC's rotation and the time consumed in its realization but enables the application of other suitable solutions already developed for the classical ECT such as multifrequency techniques, optimized signal processing, and so on.

### III. CONSIDERED TEST BED AND EXPERIMENTAL/NUMERICAL SETUPS

This section presents all the details regarding the considered test bed and the experimental/numerical setups. In particular, Section III-A presents the considered test bed with details of both the sample and crack characteristics. Section III-B describes the experimental setup with the electrical parameters and the test procedures. The developed numerical procedures with the used setting parameters are finally reported in Section III-C.

#### A. Considered Test Bed

The performance of the developed probe was evaluated considering both buried and superficial cracks on a sample of aluminum alloy (Al AW 6082). The sample has dimensions of  $200 \times 200$  mm and a thickness of 4 mm. The electrical conductivity is 27.2 MS/m.

Fig. 6 shows the main characteristics of the certified cracks under consideration. They can be characterized by their length ( $l$ ), thickness ( $t$ ), and height ( $h$ ). The crack depth ( $d$ ), defined as the distance between the top of the crack and the top of the sample under test, is an important parameter to be considered since it provides the dimension of how the defect is buried in the material. In addition, carrying out tests both on the surface where the defects are visible (superficial) and on the opposite surface where the defects are hidden (buried), subscripts  $s$  and  $b$  are used to identify on which side the test has been carried out.

The characteristics that describe the considered cracks are shown in Table I.

#### B. Experimental Setup

The experimental setup consists of six sections: signal generation and preamplification, excitation and sensing (E&S),

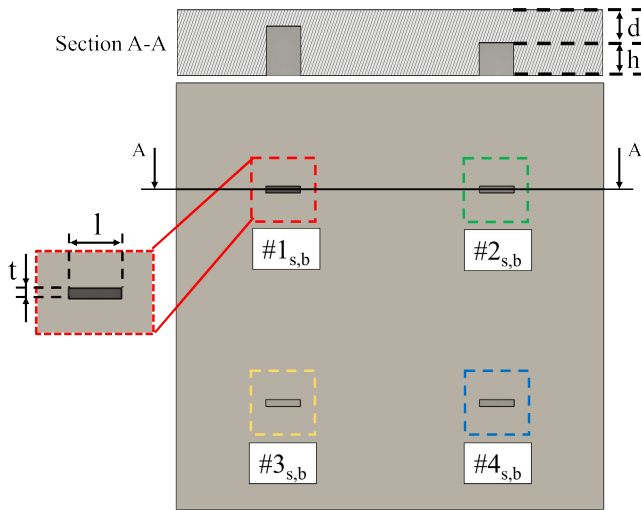


Fig. 6. Representation of the considered sample with the cracks characteristics length ( $l$ ), thickness ( $t$ ), height ( $h$ ), and depth ( $d$ ) of the crack.

TABLE I

MAIN CHARACTERISTICS OF ANALYZED CRACKS. THE SUBSCRIPTS  $s$  AND  $b$  IDENTIFY THE SUPERFICIAL AND BURIED CRACKS, RESPECTIVELY

Defect name	$l$ [mm]	$t$ [mm]	$h$ [mm]	$d$ [mm]
#1 <sub>s</sub>			3	0
#2 <sub>s</sub>			2	0
#3 <sub>s</sub>			1.5	0
#4 <sub>s</sub>	5	0.1	1	0
#1 <sub>b</sub>			3	1
#2 <sub>b</sub>			2	2
#3 <sub>b</sub>			1.5	2.5
#4 <sub>b</sub>			1	3

power supply, signal conditioning, and data acquisition and management.

The signal generation and preamplification section is composed of two bipolar power amplifiers (Kepco BOP 20-20M) fed by a two-channel signal generator (Siglent SDG1032X). This section is necessary in order to have a current-controlled system and to amplify the excitation currents. The root mean square values of the two excitation currents are measured using two current meters (Rigol DM3058). The E&S section consists of the two excitation coils (fed by the amplified excitation currents) that generate the rotating induced currents and a triaxial TMR sensor (composed of three single TMR sensors [19]) that measures the magnetic induced fields in the  $x$ - $y$ - $z$ -directions as already extensively described in Section II. The triaxial TMR is powered by a dc power supply constituting the power supply section (Agilent E3631A) with a voltage of +6 V. Thanks to its two separate output ports, the same dc power supply is used to feed three instrumentation amplifiers (Analog Devices AD620) with a voltage of  $\pm 16$  V. These instrumentation amplifiers make up the signal conditioning section and are used to amplify the output signals from the triaxial TMR. The signal acquisition circuitry for the TMR sensors is shown in Fig. 7. The ac coupling of each operation amplifier was realized by means of a resistance  $R$  of 1 k $\Omega$

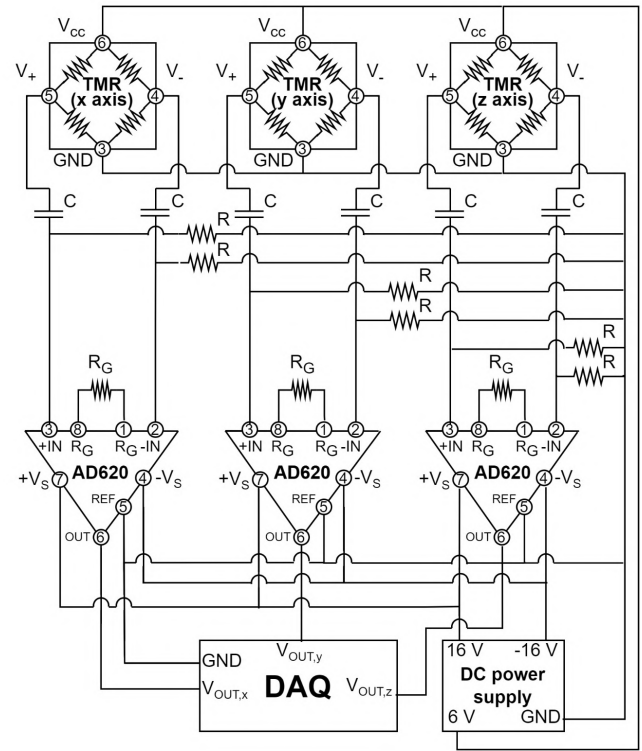


Fig. 7. Representation of the signal conditioning and acquisition circuit for the three TMR sensors.

and a capacitance  $C$  of 470 nF. A gain resistance  $R_G$  equal to 1 k $\Omega$  allows setting an amplifier gain equal to 50.

The output signals of the three instrumentation amplifiers are digitized by means of a National Instruments data acquisition DAQ card (NI USB-6212), which composes the data acquisition section. The DAQ card supports up to 16 analog input channels, a maximum sampling frequency of 400 kS/s with a resolution of 16 bits.

The realized probe was mounted on the arm of a precision movement system managed via the RS-232 communication bus. The movement system allows the scanning of a  $300 \times 300$  mm area with a resolution of 0.1 mm. The experimental tests were executed following a regular scan path of  $40 \times 40$  mm with a step of 1 mm, as shown in Fig. 8.

The management section consists of a personal computer, running a LabView-based automation software. It allows setting the scanning parameters (speed, step, and area to be scanned on the analyzed sample), the sampling frequency, and the number of points to be acquired. Finally, the data are stored and processed using suitable software developed in MATLAB environment. It performs the fast Fourier transform (FFT) to evaluate the amplitude of the three acquired voltage signals and some suitable figures of merit, as better detailed in Section IV.

The block diagram of the adopted experimental setup is shown in Fig. 9, while the pictures of the actual experimental setup with details of the signal conditioning, data acquisition, and E&S sections are illustrated in Fig. 10.

The tests have been carried out by supplying the two excitation coils with sinusoidal signals of different amplitudes

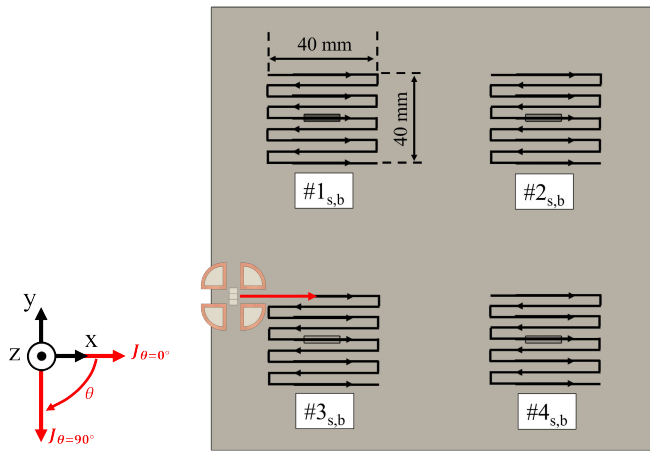


Fig. 8. Representation of the scan path considered and the orientation of ECs in the case of scanning for the considered defects.

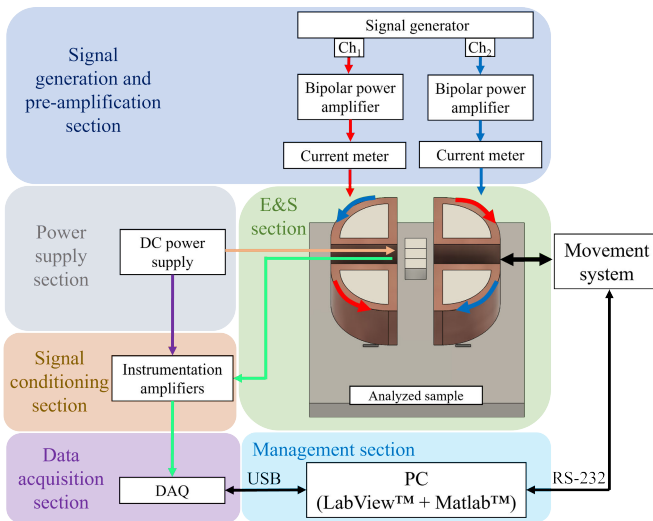


Fig. 9. Block diagram of the adopted experimental setup.

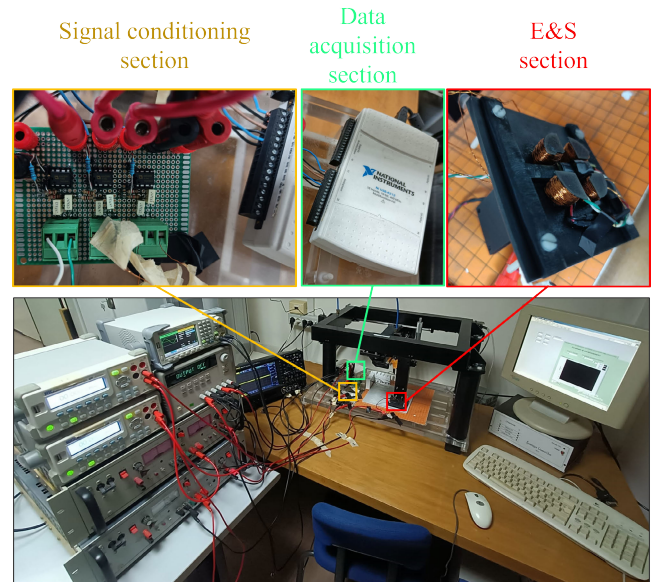
at a frequency of 500 Hz. The excitation frequency was chosen in order to guarantee penetration of the induced currents (skin depth equal to 4.3 mm) suitable for the considered test samples (characterized by a thickness of 4 mm).

The rms values of the currents supplying the excitation coils have been chosen in order to allow the desired changes in the ECs' orientation angles applying (3) and (4) considering a base current  $I_b$  with an rms value equal to 300 mA. The adopted rms current values with the corresponding ECs' orientation angles are reported in Table II.

Fig. 8 shows a graphical representation of the orientation angles  $\theta$  of the EC respect to the orientation of the defects described in Fig. 6 and Table I.

### C. Numerical Setup

The proposed probe detection capability has been tested also in a simulation environment by means of finite element analysis (FEA) in COMSOL Multiphysics 6.0. The physics interface "magnetic fields" of COMSOL Multiphysics has been adopted to evaluate the magnetic induction around the conductive plate. In the simulation, the probe scanning, as described in



Adopted experimental set-up

Fig. 10. Pictures of the developed experimental setup with details of signal conditioning, data acquisition, and E&S sections.

TABLE II  
RMS VALUES OF THE USED EXCITATION CURRENTS TO OBTAIN THE CONSIDERED ECs' ORIENTATION ANGLES

ECs orientation angle ( $\theta$ ) [°]	$I_1$ [mA]	$I_2$ [mA]
0	300	-300
30	409.81	-109.81
60	409.81	109.81
90	300	300

Section III-B, is realized by means of a parametric sweep, varying the position of the ECT probe and maintaining the other geometry entities fixed. For each probe position, the FEA simulation is repeated, and the 3-D magnetic field components are extracted at each sensitivity point of the three magnetic sensors (see Fig. 1).

The numerical evaluation allows for extending the analysis of the ECT response of the novel probe in different conditions, and it allows for investigating defects at any depth. In the experimental campaign, only the cracks at the top or at the bottom of the conductive sample were analyzed, as explained in Section III-A. The realization of buried defects with different depths is more complex and expensive; therefore, the numerical analysis allows investigating a greater number of different defects in an easier and cheaper way.

The crack #4, characterized by the smallest height, has been selected for a deep analysis, considering different excitation currents and different defect depths. In detail, the crack #4 was analyzed varying the depth with a step of 1 mm from the superficial positioning (#4<sub>s</sub>) to the buried one (#4<sub>b</sub>). The numerical analysis was repeated for different ECs' orientations from 0° to 90° with a step of 10°.

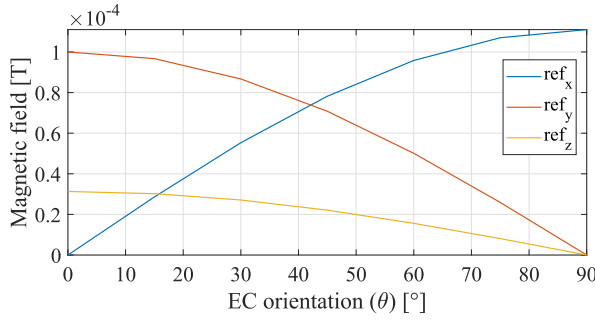


Fig. 11. Spatial components of magnetic field reference values versus the ECs' orientation angles in the absence of the defect in the center of the conductive sample.

#### IV. NUMERICAL AND EXPERIMENTAL RESULTS

The result of the scanning operation described above consists of a set of maps that represent the variation, due to the crack presence, of the magnetic field around each considered defect. In the case of simulated maps, these are the values of the simulated magnetic field, while, in the case of experimental maps, the values are reported in terms of the amplitude of the output voltages related to the three considered TMR sensors.

A suitable figure of merit was identified to quantify the detection capability of the novel probe. The figure of merit  $P$  is formulated as follows:

$$P_{x,y,z} = \frac{(\max - \text{ref})}{\text{ref}} \cdot 100 \quad (5)$$

where  $\max$  is defined as the maximum value recorded in the map due to the crack presence, and  $\text{ref}$  is the reference value defined as the mean of the boundary values of the map (where the effect of the crack presence on the magnetic field is negligible). The defined figure of merit  $P_{x,y,z}$  allows us to quantify the maximum percentage variation of the simulated/measured magnetic field due to the crack presence.

##### A. Numerical Results

Initially, an analysis of the magnetic field sensed by the novel probe in the absence of the defect was carried out, investigating the trends of the expected reference values  $\text{ref}$  of the measured magnetic field.

Fig. 11 illustrates the reference values  $\text{ref}_{x,y,z}$  of the three spatial components of the magnetic field for the considered ECs' orientation angles from  $0^\circ$  to  $90^\circ$ .

The values of  $\text{ref}_x$  and  $\text{ref}_y$  show a symmetric trend since to rotate the ECs on the  $x$ - $y$  plane from  $0^\circ$  to  $90^\circ$ , and a reduction of the  $y$ -component of the excitation magnetic field occurs with a simultaneous increase in the corresponding  $x$ -component. The nonperfect symmetry between the two trends can be related to the different positions of the  $x$  and  $y$  sensitivity points of the magnetic field sensors (see Section II).

In ideal conditions, where the sensitivity point of the magnetic field sensor along the  $z$ -axis could be located symmetric respect to the probe geometry, the reference value on  $z$ -axis should be not affected by the ECs' orientation since it is realized on the  $x$ - $y$  spatial plane. The observed small variations of the reference value on the  $z$ -axis respect to the ECs' orientation

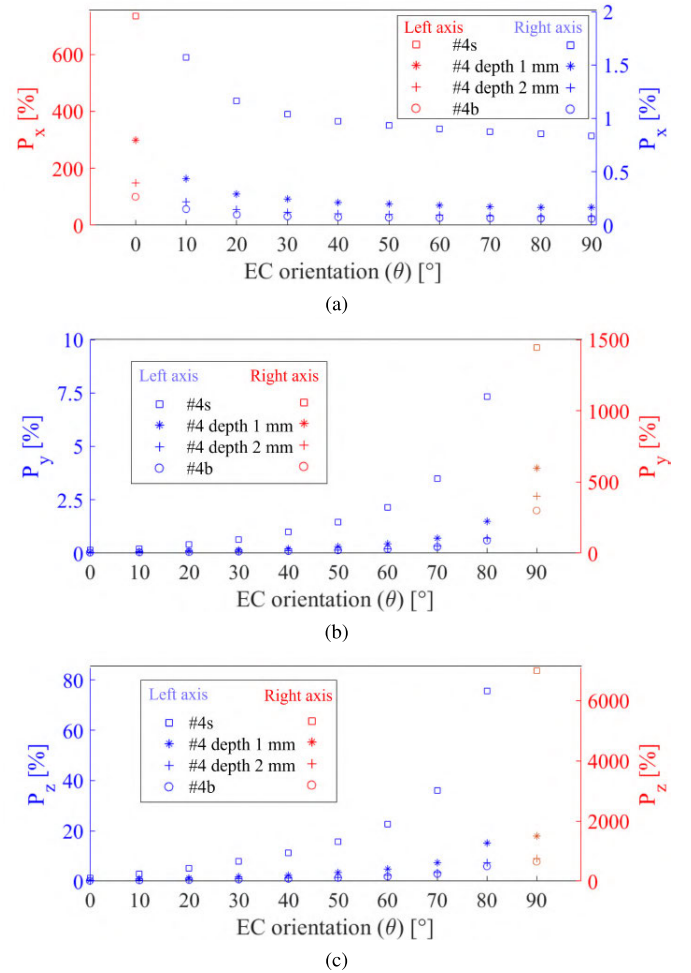


Fig. 12. Trend of the figure of merit ( $P_{x,y,z}$ ) considering crack #4 positioned at different positions. Magnetic flux density in (a)  $x$ -direction ( $B_x$ ), (b)  $y$ -direction ( $B_y$ ), and (c)  $z$ -direction ( $B_z$ ). The two axes show different value ranges.

are then related to 3 mm of asymmetry in the location of the  $z$ -axis sensitivity point.

Looking at Fig. 11, it is important to remark that as in the case of an ECs' orientation of  $0^\circ$  for  $\text{ref}_x$  and  $90^\circ$  for  $\text{ref}_y$  and  $\text{ref}_z$ , the achieved values became very low (some  $nT$ ). In these conditions, the reference values to be used in the evaluation of the defined figure of merit  $P_{x,y,z}$  are near zero, generating an important increase in the figure of merit not really connected to a corresponding improvement in the probe performance.

After this brief analysis of the probe response in the absence of defects, the numerical results, obtained considering the crack #4 at different depths and different orientation angles, are reported in the following. In particular, the values of the figure of merit extracted from the FEA simulations data are reported in Fig. 12 for each spatial component of the magnetic field. A second axis was adopted for the figure of merit values calculated on the magnetic field maps characterized by a near-zero reference value.

Looking at the numerical results shown in Fig. 12, the first important aspect to remark is related to the capability of the proposed probe to detect also the smallest and deepest crack #4<sub>b</sub>. The increase in ECT probe detection performance

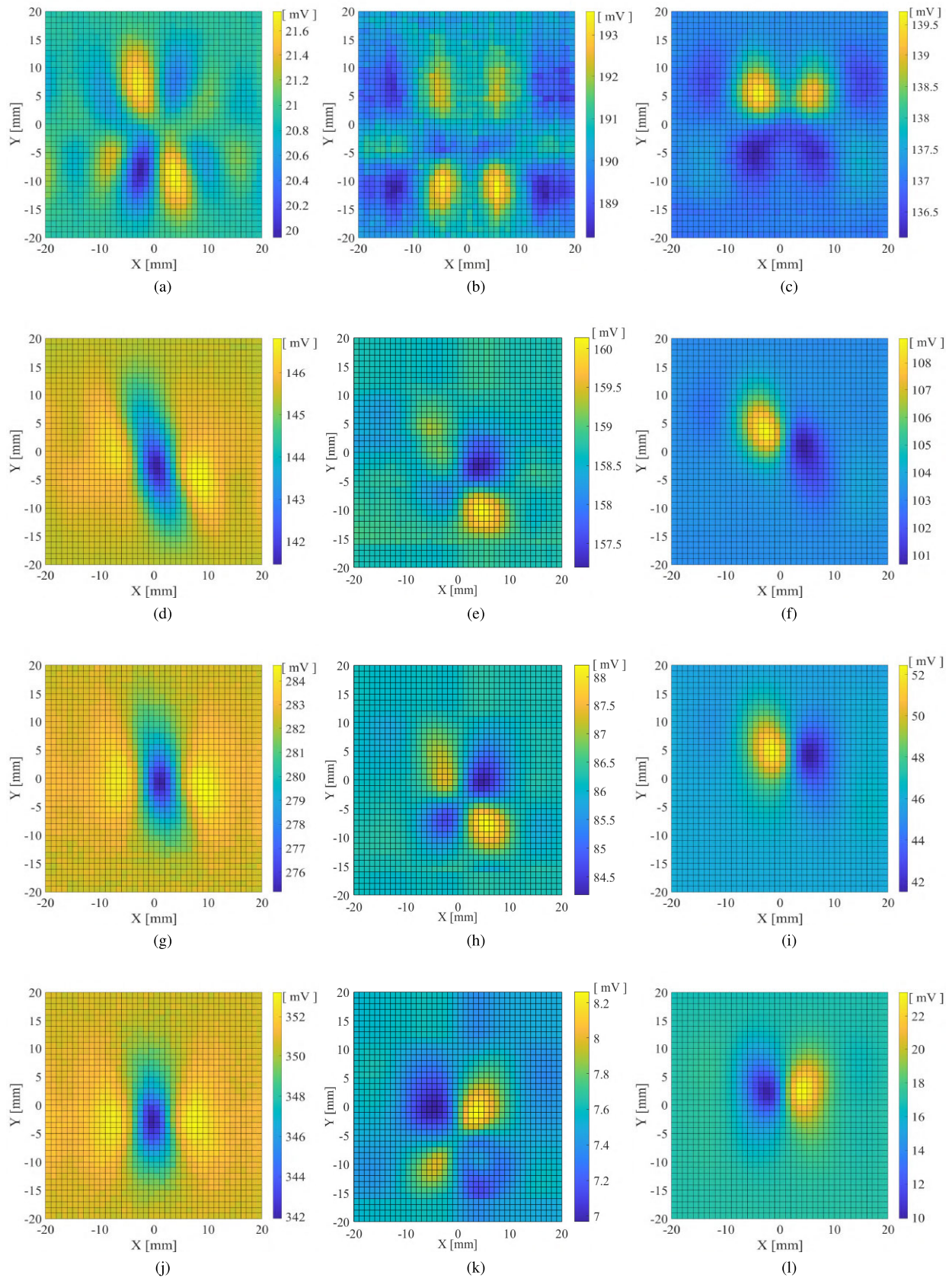


Fig. 13. Induced voltage (TMR output) experimental maps on (a), (d), (g), and (j) x, (b), (e), (h), and (k) y, and (c), (f), (i), and (l) z sensing axis in the presence of a superficial defect #1<sub>s</sub>, characterized by an EC direction of (a)–(c)  $0^\circ$ , (d)–(f)  $30^\circ$ , (g)–(i)  $60^\circ$ , and (j)–(l)  $90^\circ$ .

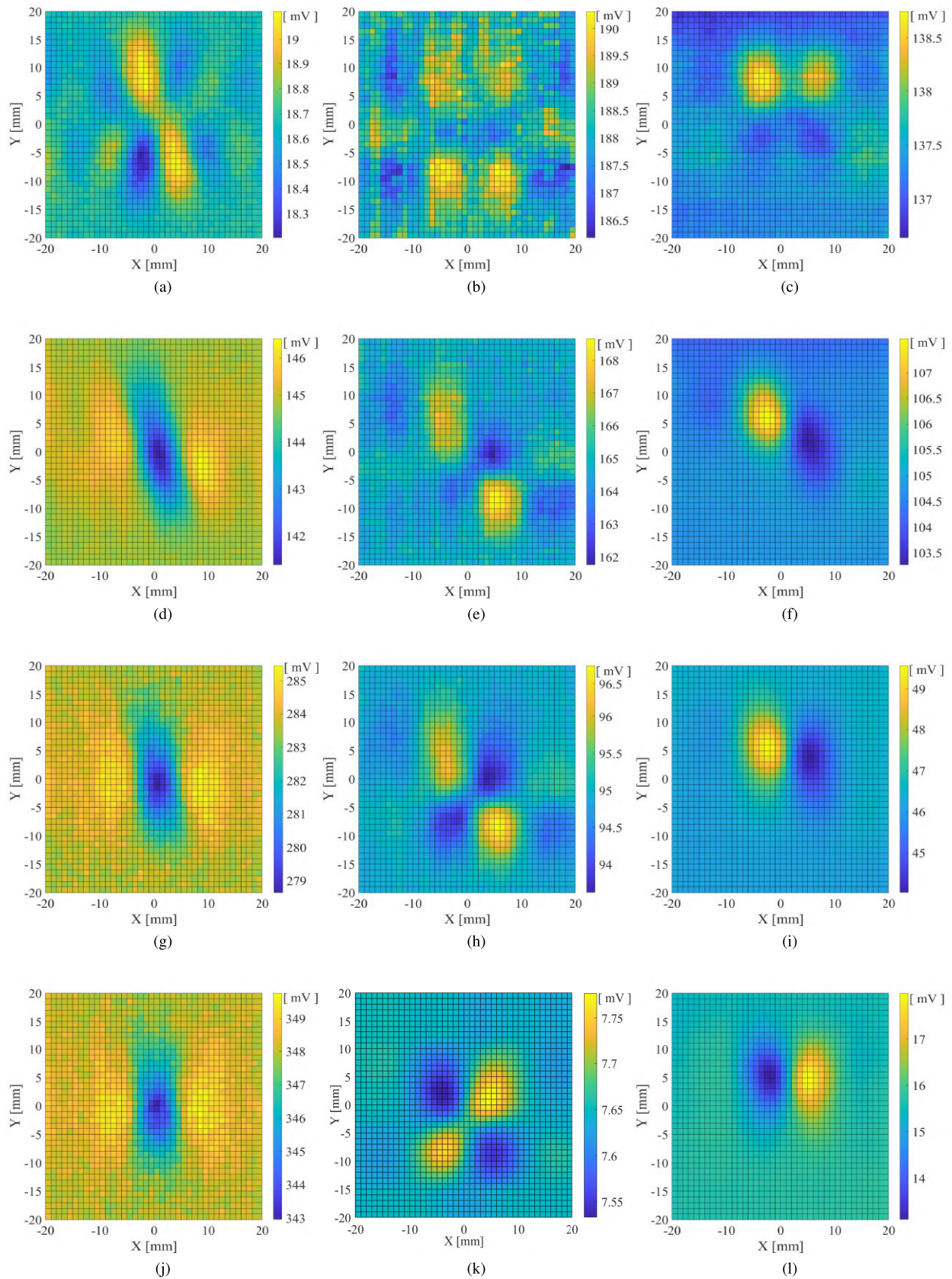


Fig. 14. Induced voltage (TMR output) experimental maps on (a), (d), (g), and (j) x, (b), (e), (h), and (k) y, and (c), (f), (i), and (l) z sensing axis in the presence of a buried defect #4<sub>b</sub> characterized by an EC direction of (a)–(c) 0°, (d)–(f) 30°, (g)–(i) 60°, and (j)–(l) 90°.

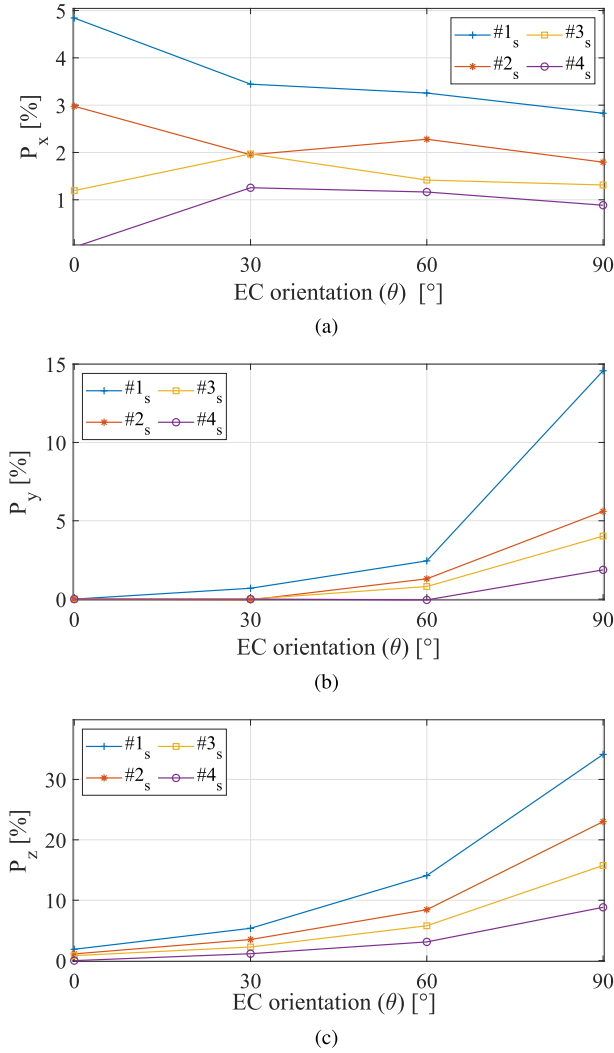


Fig. 15. Trend of the considered figure of merit ( $P_{x,y,z}$ ) for all the considered superficial defects. Induced voltage in (a)  $x$ -direction ( $V_x$ ), (b)  $y$ -direction ( $V_y$ ), and (c)  $z$ -direction ( $V_z$ ).

with the adjustment of ECs' orientation is relevant: considering the cases with nonzero reference values,  $P_z$  ranges from 5.9% to 75.5%,  $P_y$  from 0.6% to 7.3%, and  $P_x$  from 0.2% to 1.6%. The best performance is recorded for the  $z$ -component, while the worst one is recorded for the  $x$ -component. The variation of  $P_x$  with respect to the ECs' orientation is very small; this is due to the spatial position of the crack, whose main dimension is in the analysis on the  $x$ -axis.

The authors carried out another set of numerical tests in which only the position of the crack on the  $x$ - $y$  plane was modified. Comparing the results in which the main dimension of the crack is on the  $x$ -axis or the  $y$ -axis, the trends of  $P_x$  and  $P_y$  are reversed. This analysis suggests that according to the spatial position of the crack, the probe detection capabilities sensing the magnetic field component on the  $x$ -axis and the  $y$ -axis are complementary. The detection performance on the  $z$ -axis is not affected by the crack rotation on the  $x$ - $y$  plane.

### B. Experimental Results

By using the experimental setup described in Section III-B, an experimental campaign was carried out to demonstrate the

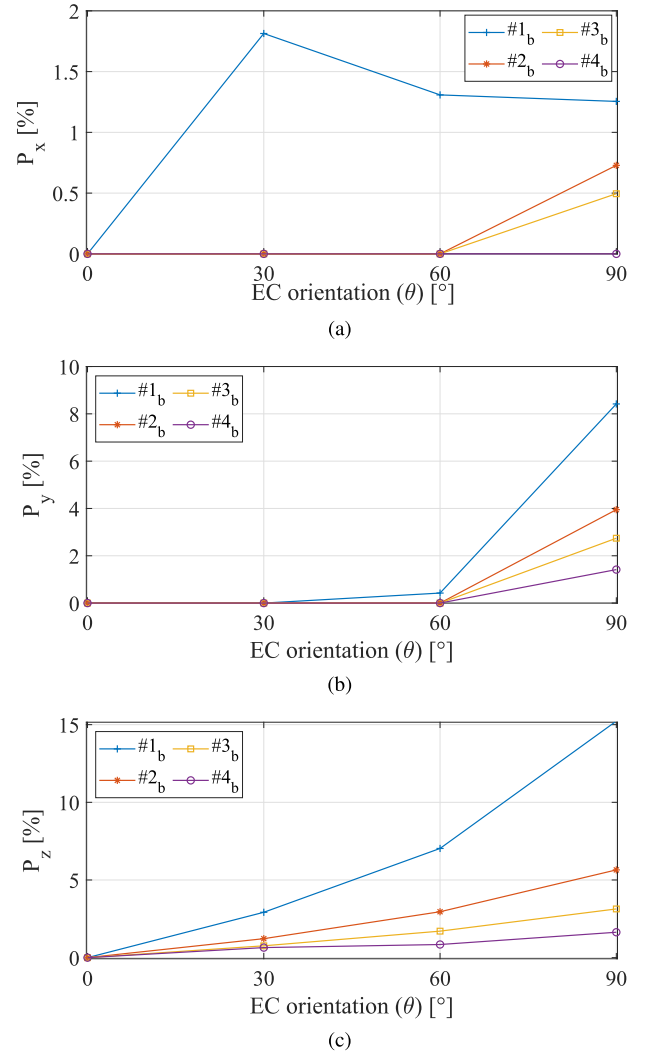


Fig. 16. Trend of the considered figure of merit ( $P_{x,y,z}$ ) for all the considered buried defects. Induced voltage in (a)  $x$ -direction ( $V_x$ ), (b)  $y$ -direction ( $V_y$ ), and (c)  $z$ -direction ( $V_z$ ).

goodness of the proposal for the detection of buried cracks of any orientation.

Several experimental tests are carried out scanning all the defects detailed in Table I and using all the ECs' orientation angles defined in Table II. The corresponding  $x$ -,  $y$ -, and  $z$ -axis magnetic field responses are then obtained. For the sake of brevity, Figs. 13 and 14 illustrate only the experimental maps on  $x$ ,  $y$ , and  $z$  sensing axes for the EC direction of  $0^\circ$ ,  $30^\circ$ ,  $60^\circ$ , and  $90^\circ$  in the presence of the bigger and superficial (#1<sub>s</sub>) and for the smaller and deepest (#4<sub>s</sub>) cracks, respectively.

The experimental maps highlight how the novel 4Q probe is able to detect all the defects under analysis. The capability detection of the novel probe is confirmed by the figure of merit values evaluated on the experimental maps. The trends of the figure of merit are shown in Fig. 15 in the case of superficial cracks and Fig. 16 in the case of buried cracks.

As expected, crack visibility improves as the orientation of the ECs increases from  $0^\circ$  to  $90^\circ$ . It demonstrates the new probe's suitability to detect arbitrarily oriented cracks. As an example, considering the case of buried cracks, the variation

of ECs' orientation allows to pass from  $P_z$  values near to zero in the case of  $0^\circ$  to 15.2% in the case of  $90^\circ$  for the crack #1<sub>b</sub>, 5.6% for crack #2<sub>b</sub>, 3.1% for crack #3<sub>b</sub>, and 1.6% for crack #4<sub>b</sub>.

The presence of the cracks in the conductive sample is more clear and evident for the maps on the  $z$  sensing axis, whereas the worst results are recorded for the maps on the  $x$  sensing axis, confirming the considerations already made on numerical tests. In the case of superficial cracks, the values of  $P_z$  range from 8.8% to 34.1%, the value of  $P_y$  range from 1.9% to 14.6%, and the values of  $P_x$  range from 0.9% to 2.8% (see Fig. 15). In the case of buried cracks, the values of  $P_z$  range from 1.6% to 15.2%, the values of  $P_y$  range from 1.4% to 8.4%, and the values of  $P_x$  range from 0.05% to 1.3% (see Fig. 16).

The experimental results, in accordance with the numerical ones, demonstrated the suitability of the novel 4Q probe to detect small and buried cracks with any orientation. As expected, the probe's performance is better in the case of cracks characterized by a greater size and lower depth. According to the identified figure of merit, the best performance is always obtained in the case of superficial cracks, except in the case of #4<sub>s</sub>, for which  $P_z$  is equal to the 8.8%, with respect to the case of #1<sub>b</sub>, where  $P_z$  is equal to the 15.2%. In this last case, the performance improvements due to the bigger defect height are dominant with respect to the smaller value of the defect depth. Although a specific experimental analysis of the performances of the proposed solution for defects of different lengths has not been presented, some considerations can be made taking into account the general behavior of ECT techniques. Considering the limited length (5 mm) of the investigated cracks, it is possible to state that the defect detection capability increases with the defect length. This behavior shows a saturation effect when the defect length overcomes a limit defined according to the EC extent. Finally, the benefits of the application of (any) REC technique reduce with the decrease in the defect length due to the lower effect of the ECs' orientation on the ECs perturbation due to the defect presence.

In conclusion, as shown in Fig. 14 when the defects are more difficult to detect (smaller in size and positioned deeper in the material), the effect of the application of the REC technology is more evident. In fact, looking at Fig. 14(b) and (e), referring to the deepest (and smaller in height) defect considered in the conducted experimental campaign, if the wrong orientation angle is used, the defect could not be detected: the obtained magnetic field maps do not show the peaks related to the defect presence due to the noise present. Considering the results obtained on the  $z$ -axis [see Figs. 14(c)–(l) and 16(c)], the defect detection capabilities are demonstrated for all the considered defects and orientation angles. This also enables the possibility to check the applicability of the proposed solution for smaller and deeper defects.

As a final remark, the detection performance in the case of sensing the  $z$ -axis component of the magnetic field suggests investigating the possibility of designing a new single-axis probe in which the reduction of the number of magnetic sen-

sors could reduce the size and weight of the probe. Moreover, the possibility of reducing the distance among the excitation coils could improve the magnetic field penetration in the conductive sample, increasing the probe detection capability.

## V. CONCLUSION

This work proposes a new ECT probe designed to identify small buried cracks with arbitrary orientations in conductive materials. The novel probe uses two pairs of coils and an amplitude modulation of the excitation currents to rotate the path of ECs within the conductive sample. With the aim to also perform a performance comparison of three different magnetic sensitivity axes, the detection system was realized by three single-axis TMR sensors, allowing a 3-D measurement of the sensed magnetic field. To validate the effectiveness of the proposal, numerical tests followed by an extensive experimental campaign have been carried out. In addition, a comprehensive analysis was performed, comparing the performance of the proposed probe on the three sensitivity axes for various crack heights and depths on a 4-cm conductive specimen. The results showed that the novel probe is able to detect hidden defects up to a depth of 3 mm with a minimum height of 1 mm. For all three sensitivity axes, an improvement was clearly observed in the defect detection capability with respect to the orientation angle between the defect and the EC's path, even if the best performances were always observed on the axes orthogonal to the specimen ( $z$ -axis). The detection capabilities, as expected, showed better performance in the case of cracks characterized by a greater size and lower depth. Considering the buried cracks that are the most difficult to detect, especially when applying REC techniques, the change in the EC orientation produced a significant variation in the considered figure of merit. In particular, for the deepest (3 mm depth) and smallest crack (5 mm length and 1 mm height) under investigation, the figure of merit on the  $z$  sensitivity axis showed changes from 0.05% for an EC's orientation angle of  $0^\circ$  to 1.3% for  $90^\circ$ . It is important to note that the application of (any) ECT technique may not provide benefits by decreasing defect length. In fact, as a general behavior of ECT techniques, decreasing defect length reduces detection performance. In future research activities, the authors will explore the possibility of improving probe performances by reducing the number of magnetic sensors (using only the  $z$ -axis) and enabling a more detailed probe design by analyzing different probe sizes and different shapes of the used coils. Furthermore, different REC technologies with a multifrequency approach will be investigated to increase the detection capabilities.

## REFERENCES

- [1] L. Peng, C. Ye, Y. Tao, C. Long, and M. Li, "Inspection of the undulation structure with an in-plane differential flexible array probe," in *Proc. IEEE 8th Int. Workshop Metrol. Aerosp.*, Jun. 2021, pp. 547–551.
- [2] J. C. Aldrin, J. S. Knopp, E. A. Lindgren, and K. V. Jata, "Model-assisted probability of detection evaluation for eddy current inspection of fastener sites," in *Proc. AIP Conf.*, Mar. 2009, vol. 1096, no. 1, pp. 1784–1791.
- [3] B. Yilmaz, A. Ba, E. Jasiuniene, H. K. Bui, and G. Berthiau, "Comparison of different non-destructive testing techniques for bonding quality evaluation," in *Proc. IEEE 5th Int. Workshop Metrol. Aerosp.*, Jun. 2019, pp. 92–97.

- [4] J. García-Martín, J. Gómez-Gil, and E. Vázquez-Sánchez, "Non-destructive techniques based on eddy current testing," *Sensors*, vol. 11, no. 3, pp. 2525–2565, Feb. 2011.
- [5] H. E. Farag, E. Toyserkani, and M. B. Khamesee, "Non-destructive testing using eddy current sensors for defect detection in additively manufactured titanium and stainless-steel parts," *Sensors*, vol. 22, no. 14, p. 5440, Jul. 2022.
- [6] L. Ferrigno, M. Laracca, H. Malekmohammadi, G. Y. Tian, and M. Ricci, "Comparison of time and frequency domain features' immunity against lift-off in pulse-compression eddy current imaging," *NDT E Int.*, vol. 107, Oct. 2019, Art. no. 102152.
- [7] C. Ye, Y. Huang, L. Udpa, and S. S. Udpa, "Novel rotating current probe with GMR array sensors for steam generate tube inspection," *IEEE Sensors J.*, vol. 16, no. 12, pp. 4995–5002, Jun. 2016.
- [8] A. Sardellitti, F. Milano, M. Laracca, S. Ventre, L. Ferrigno, and A. Tamburrino, "An eddy-current testing method for measuring the thickness of metallic plates," *IEEE Trans. Instrum. Meas.*, vol. 72, pp. 1–10, 2023.
- [9] A. Sardellitti, G. D. Capua, M. Laracca, A. Tamburrino, S. Ventre, and L. Ferrigno, "A fast ECT measurement method for the thickness of metallic plates," *IEEE Trans. Instrum. Meas.*, vol. 71, pp. 1–12, 2022.
- [10] A. Tamburrino, A. Sardellitti, F. Milano, V. Mottola, M. Laracca, and L. Ferrigno, "Old but not obsolete: Dimensional analysis in non-destructive testing and evaluation," *NDT E Int.*, vol. 141, Jan. 2024, Art. no. 102977.
- [11] J. Ge, F. Yu, T. Tomizawa, H. Song, and N. Yusa, "Inspection of pitting corruptions on weld overlay cladding using uniform and rotating eddy current testing," *IEEE Trans. Instrum. Meas.*, vol. 70, pp. 1–10, 2021.
- [12] S. Gholizadeh, "A review of non-destructive testing methods of composite materials," *Proc. Struct. Integrity*, vol. 1, pp. 50–57, Jan. 2016.
- [13] Z. Zhou, M. Qin, Y. Xie, J. Tan, and H. Bao, "Experimental study of microstructures in bias weld of coiled tubing steel strip with multi-frequency eddy current testing," *IEEE Access*, vol. 8, pp. 48241–48251, 2020.
- [14] S. Xu, V. V. Larionov, A. Soldatov, and J. Chang, "Analysis for hydrogen concentration in titanium alloys using multifrequency eddy current," *IEEE Trans. Instrum. Meas.*, vol. 70, pp. 1–8, 2021.
- [15] H. Malekmohammadi, A. Migali, S. Laureti, and M. Ricci, "A pulsed eddy current testing sensor made of low-cost off-the-shelf components: Overview and application to pseudo-noise excitation," *IEEE Sensors J.*, vol. 21, no. 20, pp. 23578–23587, Oct. 2021.
- [16] Z. Duan, Y. Kang, Y. Chen, Z. Wan, and S. Wang, "Reduction of lift-off effect in pulsed eddy current testing for surface hardness classification of ferromagnetic steel," *Measurement*, vol. 205, Dec. 2022, Art. no. 112191.
- [17] Y. Gong, X. Huang, Z. Liu, F. Deng, Y. Wu, and C. He, "Development of a cone-shaped pulsed eddy current sensor," *IEEE Sensors J.*, vol. 22, no. 4, pp. 3129–3136, Feb. 2022.
- [18] G. Betta, L. Ferrigno, M. Laracca, A. Rasile, and S. Sangiovanni, "A novel TMR based triaxial eddy current test probe for any orientation crack detection," *Measurement*, vol. 181, Aug. 2021, Art. no. 109617.
- [19] *TMR2905 Ultra High Sensitivity TMR Linear Sensor*. Accessed: Aug. 4, 2023. [Online]. Available: <http://www.dowaytech.com/en/1401.html>
- [20] N. Zhang, C. Ye, L. Peng, and Y. Tao, "Novel array eddy current sensor with three-phase excitation," *IEEE Sensors J.*, vol. 19, no. 18, pp. 7896–7905, Sep. 2019.
- [21] C. Ye, Y. Wang, and Y. Tao, "High-density large-scale TMR sensor array for magnetic field imaging," *IEEE Trans. Instrum. Meas.*, vol. 68, no. 7, pp. 2594–2601, Jul. 2019.
- [22] M. Lu et al., "Determination of surface crack orientation based on thin-skin regime using triple-coil drive-pickup eddy-current sensor," *IEEE Trans. Instrum. Meas.*, vol. 70, pp. 1–9, 2021.
- [23] Y. Wang, C. Ye, and M. Wang, "Synthetic magnetic field imaging with triangle excitation coil for inspection of any orientation defect," *IEEE Trans. Instrum. Meas.*, vol. 69, no. 2, pp. 533–541, Feb. 2020.
- [24] N. Zhang, C. Ye, L. Peng, and Y. Tao, "Eddy current probe with three-phase excitation and integrated array tunnel magnetoresistance sensors," *IEEE Trans. Ind. Electron.*, vol. 68, no. 6, pp. 5325–5336, Jun. 2021.
- [25] D. Y. Um and G. S. Park, "DC-Magnetization-Based eddy current testing for arbitrary orientation defects detection in ferromagnetic steel," *IEEE Trans. Magn.*, vol. 59, no. 5, pp. 1–4, May 2023.
- [26] L. Xiucheng, Y. Jieming, W. Bin, and H. Cunfu, "A novel generation method of oscillatory rotating eddy current for crack orientation determination and detection in metal plates," *NDT E Int.*, vol. 97, pp. 1–10, Jul. 2018.
- [27] J. Ge, B. Hu, C. Yang, F. Yu, and N. Yusa, "Surface profile reconstruction of complex cracks using the signals of rotating eddy current testing through the eddy current imaging method," *IEEE Trans. Ind. Electron.*, vol. 70, no. 9, pp. 9632–9641, Sep. 2023.
- [28] J. Ge, C. Yang, F. Yu, and N. Yusa, "Transformation of the rotating eddy current testing signal at the desired eddy current orientation," *NDT E Int.*, vol. 125, Jan. 2022, Art. no. 102551.
- [29] T. Theodoulidis, N. Poulakis, and A. Dragogias, "Rapid computation of eddy current signals from narrow cracks," *NDT E Int.*, vol. 43, no. 1, pp. 13–19, Jan. 2010.
- [30] X. Li, G. Tian, K. Li, H. Wang, and Q. Zhang, "Differential ECT probe design and investigation for detection of rolling contact fatigue cracks with different orientations," *IEEE Sensors J.*, vol. 22, no. 12, pp. 11615–11625, Jun. 2022.
- [31] Z. Xu, X. Wang, and Y. Deng, "Rotating focused field eddy-current sensing for arbitrary orientation defects detection in carbon steel," *Sensors*, vol. 20, no. 8, p. 2345, Apr. 2020.
- [32] D. J. Pasadas, A. L. Ribeiro, H. G. Ramos, and T. J. Rocha, "Inspection of cracks in aluminum multilayer structures using planar ECT probe and inversion problem," *IEEE Trans. Instrum. Meas.*, vol. 66, no. 5, pp. 920–927, May 2017.
- [33] A. Bernieri, L. Ferrigno, M. Laracca, and A. Rasile, "Eddy current testing probe based on double-coil excitation and GMR sensor," *IEEE Trans. Instrum. Meas.*, vol. 68, no. 5, pp. 1533–1542, May 2019.
- [34] F. Carere, A. Bernieri, L. Ferrigno, M. Laracca, and S. Sangiovanni, "A novel multi-excitation ECT probe for deep defects with any orientation," in *Proc. IEEE 10th Int. Workshop Metrol. Aerosp. (MetroAeroSpace)*, Jun. 2023, pp. 519–524.



**Federico Carere** (Member, IEEE) received the M.S. degree (summa cum laude) in electrical engineering and the Ph.D. degree in engineering and applied science for energy and industry from the University of Sapienza, Rome, Italy, in 2019 and 2023, respectively.

He is currently a Post-Doctoral Researcher with the Department of Astronautical, Electrical and Energy Engineering, University of Sapienza. He has authored and coauthored peer-reviewed papers in international journals and proceedings of international conferences. His current research interests include distributed measurement systems for modern electric grids, nondestructive testing based on eddy-current techniques, and sensor realization and characterization.



**Alessandro Sardellitti** (Member, IEEE) was born in Sora, Italy, in 1993.

He is currently a Post-Doctoral Researcher with the Department of Electrical and Information Engineering, University of Cassino and Southern Lazio, Cassino, Italy. His current research interests concern the development of methodologies, numerical models, and measurement setups suitable for the realization of nondestructive testing and evaluation.



**Andrea Bernieri** (Member, IEEE) received the M.S. and Ph.D. degrees in electrical engineering from the University of Naples Federico II, Naples, Italy, in 1982 and 1987, respectively.

He has been a Full Professor of electrical measurements with the Faculty of Engineering, University of Cassino and Southern Lazio, Cassino, Italy, since 2002. He is principally concerned with research into the design and realization of automatic measurement systems, development of techniques and measurement algorithms for dynamic system model

identification and characterization, development of neural algorithms for fault detection and diagnosis in dynamic systems, design and realization of eddy current testing systems, and development of techniques and instruments for measuring electric power in distorted conditions.



**Luigi Ferrigno** (Senior Member, IEEE) is currently a Full Professor of electric and electronic measurement and a Rector's Delegate for the technology transfer, spin-off, and start-up with the University of Cassino and Southern Lazio, Cassino, Italy. He coordinated and participated in several national and international research and technology transfer projects. His current research interests include the development of smart and distributed measurement systems and novel measurement methods in several application fields, such as energy, NDT4.0, smart

cities, the Internet of Things (IoT), and automotive and medical devices.



**Silvia Sangiovanni** was born in Rome, Italy. She received the M.S. degree in electronic engineering and the Ph.D. degree in electrical engineering from the Sapienza University of Rome, Rome, in 1990 and 1994, respectively.

Since 1995, she has been a Researcher of electrical measurement with DIAEE, Rome. Her research interests include the field of digital signal processing applied to electrical measurements, power quality, and clinical engineering. She is a member of the Italian Group on Electrical and Electronic Measurements.



**Marco Laracca** (Member, IEEE) received the M.S. degree in electrical engineering and the Ph.D. degree in electrical and information engineering from the University of Cassino and Southern Lazio, Cassino, Italy, in 2002 and 2006, respectively.

From 2006 to 2021, he was an Assistant Professor of electrical and electronic measurements with the University of Cassino and Southern Lazio. He has been the Chief of the ACCREDIA Notified Metrology Laboratory (LAT 105), Rome, Italy, since 2018. Since 2021, he has been an Associate Professor of

electrical and electronic measurements with the Sapienza University of Rome, Rome. His current research interests include the realization of the measurement system for nondestructive testing, sensor realization and characterization, electric measurement under nonsinusoidal conditions, and speed calibration.